Experimental characterisation of the thermal energy released by a Radio-Frequency Corona Igniter in Nitrogen and Air

G. Discepoli[a,*], V. Cruccolini[a], F. Ricci[a], A. Di Giuseppe[b], S. Papi[b], C. N. Grimaldi[a]

[a] *Università degli Studi di Perugia, Department of Engineering, Italy*
[b] *Federal-Mogul Powertrain Italy a Tenneco Group Company, Italy*

Abstract

The Radio-Frequency Corona Ignition System is characterised by a wide initial combustion volume and precursors production, via radical insemination by the streamers, in addition to high released thermal energy. These features lead to faster combustion, a higher tolerance for lean mixtures and EGR dilutions and, in general, more adaptability. The thermal energy released by the igniter to the surrounding medium can help to understand the performance, the behaviour and the application range. This paper proposes a systematic experimental analysis of the thermal energy released by the igniter at room temperature, via pressure-based calorimetry. This analysis, carried out at different pressures (up to 10 bar) and medium type (air or nitrogen), is extended to the whole range of the corona igniter control parameters, namely streamer duration and driving voltage. The latter is proportional to the maximum electrode voltage, as shown in the model here presented, and as confirmed by experiments.

The results show, for all the vessel pressures, the high energetic efficiency of the ignition system and the high amount of the released energy. The latter is found to increase linearly with the corona streamers duration and quickly with the driving voltage up to the streamer-to-arc transition threshold. The efficiency tends to reach a defined upper limit. For each tested point, the energy released to pure nitrogen is higher than to air, which evidences the impact of the oxygen presence under streamer exposure.

Keywords: Corona streamer, Discharge thermal energy, Thermal efficiency, Plasma assisted ignition, Pressure-based calorimetry

1. Introduction

The pressing request, in term of pollutant emissions and carbon footprint, forces the automotive industries to introduce and develop innovative technologies to allow the internal combustion engine to be competitive in the modern world market for the next years. The need for exhaust gas recirculation (*EGR*) [1] or ultra-lean combustion [2] requires the development of advanced and innovative ignition systems and strategies, by enhancing the thermal energy conversion efficiency, that increases quite linearly with λ [3], and allowing operating conditions characterised by poor pollutant emissions [4, 5]. The water injection is also an advanced technology able to improve the combustion in the modern engines for the general performance enhancement [6, 7] as well as the thermal efficiency improvement [8, 9] or the knocking control strategies [10]. All these new working conditions demand high ignition energy not available for the conventional inductive

*Corresponding author.
E-mail address: gabriele.discepoli@unipg.it; *Tel./fax:* +39 075.585.3749
Università degli Studi di Perugia, Department of Engineering, Via Duranti 67, 06125 Perugia, Italy

Nomenclature

$ACIS$	Advanced Corona Ignition System
BDV	Breakdown Voltage
CIV	Corona Inception Voltage
$\mathbf{E}$	Electric field
EGR	Exhaust Gas Recirculation
E_r	Energy released to the medium
E_s	Energy supplied to the igniter coil
FM	Federal-Mogul Powertrain Italy a Tenneco Group Company
I_s	Igniter coil current
N	Concentration of the gas particles
p_{ch}	Bomb chamber inner pressure
p_{ch}^{max}	Chamber pressure just after a streamer event
p_{ch}^{min}	Chamber pressure just before a streamer event
T_{on}	Duration of corona discharge
UniPG	University of Perugia
v_{drift}^{ion}	Ion drift velocity
v_{drift}^{el}	Electron drift velocity
V_d	Driving voltage
V_d^0	Maximum driving voltage before corona inception
V_d^{BDV}	Driving voltage at breakdown
V_d^{CIV}	Driving voltage at corona inception
V_d^{max}	Maximum driving voltage before breakdown
V_e	Electrode voltage amplitude
V_e^{BDV}	Electrode voltage amplitude at breakdown
V_e^{CIV}	Electrode voltage amplitude at corona inception
V_s	Voltage amplitude applied to the igniter coil
V_{ch}	Bomb chamber inner volume
γ	Heat specific ratio
Δp_{ch}	Pressure gradient due to a streamer event
η	Thermal efficiency of the igniter
ν_i	Frequency of the igniter current

spark plug [11]. The increase of efficiency to transfer the primary energy (i.e. the energy supplied to the igniter primary circuit) to the air–to–fuel mix is critical [12] and, at present, it is widely below the 3% [13].

The conventional spark ignition systems have limitations in obtaining a robust ignition in high pressure (boosted engine), lean or EGR-diluted environment [14]. Therefore, the rising of the energy transferred to the mix is mandatory for the spark plug system, in particular for high turbulence intensity [15, 16]. This improvement is reached, for example, through the implementation of high-energy inductive ignition systems [3, 17, 18, 19]. Unfortunately, this technology shows electrode ablation/erosion/fouling [11, 20, 21, 22] where the plug electrodes widely affect the flame kernel development [23]. Furthermore, when the lean limit is extended, then the cycle-to-cycle variability increases. The reduction of the latter condition requires even higher released energy that consequently produces a sudden drop of the efficiency [19, 3]. The early fluctuations of the thermodynamics and fluid-dynamics operating conditions around the spark region are the main causes of the cycle-to-cycle variation [24] while large flame kernels are less subject to conditioning [25]. Furthermore, dielectric insulation becomes an issue once higher discharge voltage is required to achieve the breakdown conditions, as in the modern engines for the high levels of boosting [5].

The plasma assisted ignition is based on the non-equilibrium low-temperature plasma and is characterised by streamers emission. Under this regime the heat loss to the electrodes is negligible [26], contrary to standard spark igniter. The energy is moved efficiently to the rotational, vibrational and electronic excited states of the medium molecules [27, 28, 29]. The excited species production and their following quenching by the molecular oxygen make the gas heating fast while the oxygen is consequently dissociated in atomic oxygen [30]. This is the main mechanism for the O production together with the direct electron impact on the O_2 [27]. The O density is however reduced by the strong interaction with the water dissociation products OH and HO_2, capable to capture the O [30], of a particular interest in the water injection case. Fundamentally, the oxygen in atomic, ionic or excited state seems to be the key chemical species for the plasma ignition [31, 32, 33], in particular in the atomic state, to increase the flame's propagation velocity [27, 34].

By means of several production mechanisms of ions and excited species [35], in particular of the highly reactive OH^* radical [36, 37], the plasma-based igniters add new paths to start a reaction chain that leads to combustion [38]. As a consequence, these igniters are characterised by the reduction of the ignition time up to two orders of magnitude [39] and the decrease of the ignition temperature [27] with respect to conventional spark igniters. More in general, this family of technologies improves the flame stability [40] and the engine performance [41, 42] thanks to the multiple spreading ignition locations of the areas of greatest active species production [43, 44, 45]. In addition, plasma-based ignition enhances the reaction kinetic due to the high electron energies [31] and to the effect on the fuel reactivity and diffusivity [46].

At present, the state-of-art plasma-assisted ignition models are lacking of accurate prevision of the released thermal energy. They have to face challenging issues [47, 48, 49] as, for example the different magnitudes order of the timescale between the plasma formation and the ignition process [48, 50]. The same streamers phenomenon is hard to model due to the complexity of the involved physics mechanisms [51, 52].

In this work, the subject of investigation is the Radio-Frequency Advanced Corona Ignition System (*RF ACIS*), based on low temperature plasma and characterised by a single electrode, fed by a 1 *MHz* AC current. It has been proved that the RF corona discharge extends the lean air–to–fuel mix combustion limit with respect to the conventional spark igniter [53, 54, 55, 56] and, as other low temperature plasma igniters, the EGR dilution tolerance [57, 58, 59]. This is possible by stabilising the combustion ignition with a large area flame kernel [60, 61] and by reducing the cycle-to-cycle variability for a given EGR rate with bigger impact on naturally aspirated loads than on boosted ones [62]. These result in an overall advantage in terms of fuel consumption and exhaust raw emissions [63].

Generally speaking, the thermal energy delivered to the charge mix is a key parameter since it heavily affects the flame kernel formation and then a proper ignition [13], as the flame kernel growth leads an essential role [64]. Indeed, the chemical activity cannot be separated from the thermal phase, even if the radicals production is supposed to be the main feature of the plasma assisted igniter. The thermal phase is spatially distributed, enhancing the chemical kinetics of the exothermic fuel oxidation, resulting in the combustion initiation [43]. Therefore, the aim of the present work is to generalise the preliminary test described in [65], on a pre-production Corona igniter element, supplied by *Federal-Mogul Powertrain Italy a Tenneco Group Company* (*FM* from now on). We adopted a systematic approach to assess the thermal energy released by the streamers to the medium (pure nitrogen, used as baseline characterisation, and air, the oxidising fluid in real working conditions). The thermal energy is measured in a simplified and controllable environment, i.e. a constant volume vessel, operated at different pressures for both the gases. The study is extended from the Corona inception voltage until the breakdown and for different duration of the discharge.

2. Experimental Layout

2.1. Advanced Corona Ignition System

The ignition system studied in this work is a pre-series model of *Advanced Corona Ignition System* (ACIS) fed by an alternating current with a frequency of about 1.04 *MHz* (RF Corona). Inside the combustion chamber, the igniter generates a strong alternating electric field magnified by the igniter tip, characterised by a small curvature radius and sharp edge [66, 67]. The electric field induces, from the four-point electrode, the production of the streamers (normally, one streamer for each electrode-point), plasma channels free to propagate inside the chamber. The streamers activate a large volume of air–fuel mixture and release a considerable amount of energy, essential for ignition in lean conditions [18, 68, 65]. The igniter is controlled by a dedicated electronic system that works as a high frequency amplifier. This system allows to set the time duration of the streamers activity T_{on} and the driving voltage V_d, the input voltage of the high frequency amplifier, to control the electric potential at the firing tip electrode. Details of the ACIS are available in our previous publications [55, 69].

2.2. Experimental setup of the released thermal energy measurement

A constant volume vessel, the *bomb*, in Plexiglas (low thermal conductivity, 0.187 $W \cdot m^{-1}K^{-1}$), accommodates the igniter tip for the released energy measurement at room temperature. The inner chamber has cylindrical geometry with a volume $V_{ch} = 22.5\ cm^3$ and allows the management of the operating conditions, i.e. temperature, pressure and gas type (air or nitrogen, 5.0 purity, *Linde*).

The measurement of the inner pressure variation Δp_{ch}, generated by the streamer discharge, is obtained by the piezoelectric low-pressure sensor *Kistler Type 7261*, with 2200 $pC \cdot bar^{-1}$ of sensitivity and $\approx 10^{-5}\ bar$ of resolution. The pressure sensor is installed at the opposite side of the igniter in the chamber and works as a ground electrode. It produces a charge signal collected by the charge amplifier *Kistler Type 5011* and converted in a proportional voltage signal. Current and voltage supplied to the igniter coil are collected by, respectively, the current probe *Teledyne LeCroy CP030* (sensitivity of 10 $mA \cdot div^{-1}$) and the passive probe *Teledyne LeCroy PP020*. A thermocouple records the temperature in the inner bomb chamber. A piezoresistive pressure transmitters *Keller PA-22S* (accuracy $\pm 1\%$ FS), once calibrated by a *Scandura Pascal 100* system, measures the initial pressure inside the chamber. All these quantities are acquired by a fast oscilloscope *Teledyne LeCroy Wavesurfer 3000* with a sampling frequency of 10 *MHz*, about ten times bigger than ACIS AC supply frequency. A pneumatic system (valves, precision pressure reducer *Festo LRP*, one-way flow controllers *Festo GR*) allows to properly control the gas pressure and the (intensive) replacement in the chamber. The medium renewal is needed before/after any test sequence as it seems the streamers products impact the igniter performance, in particular when highly electronegative and reactive species, as the oxygen, are included [70, 71], arguably due to the electrode erosion/fouling [28]. Each single discharge event is triggered by the *Arbitrary Wave Generator HP 33120A*.

2.3. Experimental setup of the igniter electric characterisation

Performance of the overall system has been evaluated analysing input and output electrical parameters. Using nitrogen (UN1066 99,9% of nitrogen) at 20 *bar* pressure, the system was stressed to simulate the operating conditions running inside an engine combustion chamber. A cylindrical constant volume vessel, made in steel AISI 316 with a tempered glass inspecting window, is used as test bench environment for system characterisation. The chamber has a constant volume of 20 mm^3. Test is performed at constant room temperature and the system, consisting of a pressure valve *Tartarini PS90A* and a pressure controller, allows to maintain the 20 *bar* during the overall test. No gas recirculation is requested during the characterisation test. A high voltage probe *Tektronix P6030A* (capacitance 3.0 pF, accuracy $\pm 3\%$) is mounted on the other side of the chamber, in physical contact with the electrode tip centre by means of a pin extender *RS 434-790*. A current probe *Tektronix TCP0030A* (accuracy $\pm 1.5\%$) and a voltage probe *Tektronix P6015A* (capacitance 3.0 pF, accuracy $\pm 3\%$) acquire current and voltage supplied to the igniter. The probes are connected to an RF cable bridge before the input coil connector. The oscilloscope *Tektronix MS056*, with a bandwidth of 350 *MHz*, acquires input and output current and voltage.

3. Methodology

3.1. Electrode voltage assessment

The analysis of the igniter electrode voltage V_e is led, along with the coil input voltage V_s and current I_s, by varying the duration T_{on} and driving voltage V_d. Actually, V_e, V_s and I_s represent the amplitude of the corresponding alternating quantity. The power input P_s is evaluated using V_s and I_s, functions of the duty

cycle. Once the igniter is mounted on the pressure bomb, pressurised at 20 *bar* in nitrogen, the oscilloscope is set with a sample rate of 1.25 GS/s to reach the accuracy on acquiring the ~ 1 *MHz* ACIS signal.
Test is divided in two phases:

- **phase 1**. Shorter T_{on} and continuous trigger impulse, necessary to analyse the power input in the igniter coil.

- **phase 2**. Longer T_{on} but a single pulse trigger to provide a more stable output voltage.

During the *phase 1*, T_{on} is set at 500 μs, the trigger input signal has a frequency f_{tr} of 25 *Hz* and V_d changes from 20 V to 50 V with steps of 10 V. Data were acquired after 5 s on each point to have a stable result. *Phase 2* has a T_{on} of 1000 μs, single pulse as trigger input signal and V_d sweep from 20 V to 50 V with 10 V step. Also in this case data is acquired after 5 s. The results are pretty well described by a linear regression (fig. 4).

Once the data are acquired, the power supplied to the igniter coil P_s is calculated considering the duty cycle acquired during the first test phase, the current I_s and the voltage V_s according to:

$$P_s = f_{tr} \cdot T_{on} \cdot V_s \cdot I_s \tag{1}$$

3.2. Thermal energy assessment

Once the external trigger starts an event, the AC current amplitude begins to rise from zero to the target level with a certain rate (fig. 1, *top*), not dependent on the particular duration selected. The streamer discharge is active as soon as the amplitude reaches a defined threshold (*CIV*, the *Corona Inception Voltage*), depending on the bomb chamber inner pressure P_{ch}, the gas type and the driving voltage V_d (and consequently the electrode voltage V_e). Correspondingly, the pressure signal shows a current–induced electromagnetic noise with an overall rise characterised by different local maxima and minima (fig. 1, *bottom*), after some tens of microseconds. This shape is consistent with the mutual interaction of sound waves propagating in the bomb chamber medium. Finally, the current falls quickly (a few tens of μs) as soon as the discharge duration reaches the assigned value. Likewise, the streamer ends once the current amplitude decreases under the *CIV* threshold. Then, the pressure signal is not affected by electromagnetic noise anymore and continues the oscillations around a well-defined average value.

The raw data of a streamer event are acquired and then processed to find the corresponding Δp_{ch}:

- a 2 *kHz* low-pass filter is applied to smooth the signal (red solid line in fig. 1, *bottom*) and remove all the noise components (well visible in the frequency domain and already described in our preliminary work [65]).

- the sections before and after the streamer event are identified to calculate, respectively, p_{ch}^{min} and p_{ch}^{max} as the average of the corresponding pressure measurement data.

Note that the proper identification of the time domain section relative to p_{ch}^{max} is critical since the pressure signal has strong oscillations and tends to decrease quickly.

The final Δp_{ch} is obtained as the mean value of 20 consecutive streamer events, produced with a frequency of 10 *Hz*, for each parameters configuration. The number of the consecutive recorded events and the streamers generation frequency are chosen as a compromise to collect as much data as possible with no visible effect on the igniter performance.

If the bomb chamber is assumed as adiabatic [13] suitable as a first approximation for few milliseconds after the streamer event), the thermal energy E_r, delivered to the chamber medium by the igniter, is given by the first law of the thermodynamics:

$$E_r = \frac{1}{\gamma - 1} V_{ch} \cdot \Delta p_{ch} \tag{2}$$

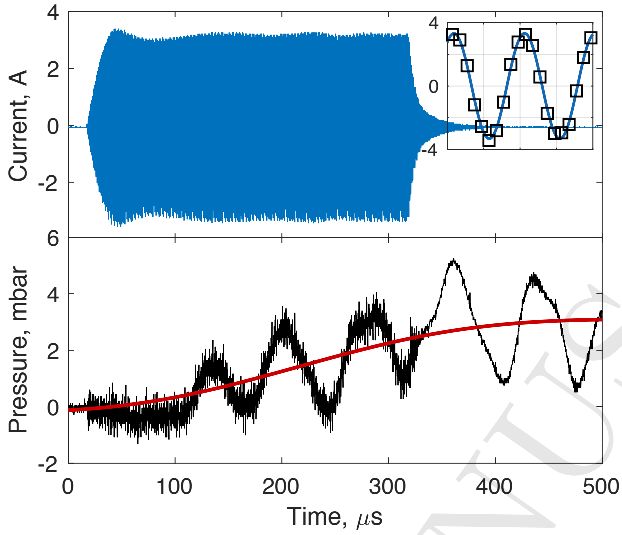

Figure 1: (*Top*) Sinusoidal current of $\approx$ 1 *MHz* produced by the ACIS igniter in a 300 μs shot and (*top right corner*) its magnification along two periods ($\approx$ 2 μs.) (*Bottom*) Pressure waves induced by the current in the bomb chamber. The solid red line represents the smoothed pressure signal once the 2 *kHz* low-pass filter is applied.

where γ is the specific heat ratio, V_{ch} is the chamber volume and $\Delta p = p_{ch}^{max} - p_{ch}^{min}$, the pressure difference before and after the streamer event, respectively.

The energy E_s supplied to the coil, or primary energy, is a function of the driving voltage V_d and of the corona duration T_{on}, in first approximation.

Experimentally, the supply current I_s and voltage V_s are simultaneously measured to determine an $E_s(V_d, T_{on})$ parametrization curve to simplify the experimental layout: once V_d and T_{on} are specified, E_s is indeed a constant of the system. The trend of the parametrization curve, as a function of V_d at fixed $T_{on} = 300\ \mu s$, is shown in fig. 2, while the dependence on T_{on} is just linear.

Finally, the thermal efficiency η characterises the capability of the igniter to transfer the primary energy to the inner chamber medium as thermal energy and is defined as the ratio between the released (thermal) energy E_r and the supplied (electric) energy E_s:

$$\eta = \frac{E_r}{E_s} \tag{3}$$

3.3. Test Campaign

The test campaign is built by varying each operating parameter, one at a time, starting from a defined set of values, addressed as *standard conditions* (tab. 1).

Table 1: Standard conditions of the operating parameters for the thermal released energy measurement.

Bomb Chamber		**Igniter**	
Gas type	Pressure	Driving voltage	Corona duration
N_2	5.5 bar	40 V	300 μs

The *corona duration* has an important role in ignition strategy since it could act as a reducer for the high *cycle-to-cycle* variability, characteristic of the ultra lean blends or high *EGR* levels [56]. This is possible at the cost of some extra energy in more stressing conditions. The operating interval of T_{on} includes values from 100 μs to 500 μs, sampled in steps of 100 μs, with the remaining parameter set as in tab. 1.

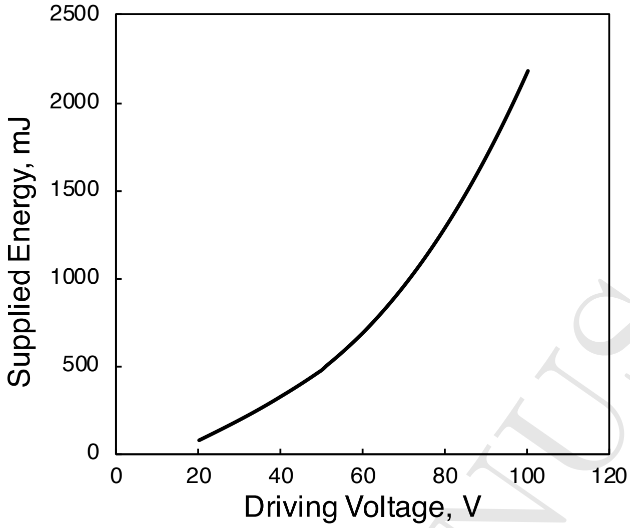

Figure 2: Parametrization curve of E_s, the energy supplied to the igniter, as a function of the driving voltage, at fixed corona duration (300 μs).

The dependence on the *driving voltage* V_d needs more care because it is strictly connected with the bomb chamber inner pressure p_{ch}. Indeed, the same test modality used for T_{on} is applied to V_d for four different chamber pressures, from 3.25 *bar* to 10 *bar* absolute, to obtain a matrix of 5×4 points. The 1 *bar* point, initially expected, was rejected because the low pressure moves up the arc event at very low V_d and directly to the igniter external metallic shell (not towards the pressure sensor). Therefore, it loses comparability with the remaining cases.

The driving voltage operating interval strongly depends on the chamber pressure p_{ch}. It has to be determined experimentally for each tested pressure, point by point, by looking for the opposite working conditions of breakdown voltage (*streamer-to-arc* transition) and corona inception voltage (minimum required for the transition to the streamer), respectively *BDV* and *CIV*, according to the nomenclature used in [72].

4. ACIS model

4.1. Model

Generally, resonant ignition systems are configured as a series-resonant *RLC* circuit but these simplified circuit models do not show a good prediction on the voltage output assessment. The reason is attributed to the stray electrical parameters in the igniter assembly. The circuit of fig. 3 represents this igniter assembly as lumped-parameter circuit and comprises:

- **a coil**. The inductance L_1 can be measured from prototypes at reasonable low frequency where capacitive effect has not contributes (normally, the impedance analyser instruments have a good electrical parameters prediction for simple *LR* circuits instead of more complicated circuit models which involve also the capacitance). The component L_1 is not purely inductive but it has some resistance, modelled separately as R_1. This value must be assessed under operating conditions where it will be many times higher than the value measured using a DC source. R_1 includes resistance representing ohmic loss, skin and proximity effects in the winding and tanδ losses in all dielectrics. Moreover, the inductor includes the C_1 parasitic capacitance between the turns. Values of R_1 and C_1 can be estimated by *FEM* analysis.

- **a firing end**. It is installed into the head of the combustion chamber and generates the corona streamers. Typically, it contributes to most of the capacitance C_L of the igniter assembly. Any

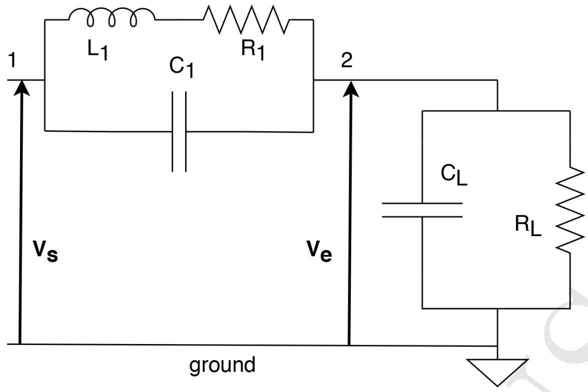

Figure 3: Scheme of the ACIS igniter assembly lumped-parameter circuit model.

component and connection between the inductor and the firing end must be considered since they can contribute significantly to the system performance. Any connection component provides additional capacitance and, consequently, as for the inductor case, an additional resistance R_L to take into account the ohmic resistance of air and bulk insulation. The R_L and the C_L, connected in parallel, represent mostly the tanδ losses in all dielectrics and the stored electrostatic energy.

Note that the lumped parameters described above may be subject to change for significantly different temperature operations.

Based on such circuit, the analytic model predicts the electrode voltage V_e as a function of the driving voltage V_d, given that V_s is proportional to V_d through the coefficient k (eq. 4). In the following, we use the complex phasor notation.

$$\overline{V}_s = k\overline{V}_d \tag{4}$$

Since

$$\overline{V}_s = \overline{V}_{12} + \overline{V}_e \tag{5}$$

where

$$\begin{aligned} \overline{V}_{12} &= \overline{Z}_1\overline{I} \\ \overline{V}_e &= \overline{Z}_2\overline{I} \end{aligned} \tag{6}$$

then

$$\overline{V}_e = \frac{\overline{V}_s}{\left[\dfrac{1}{1+\dfrac{1}{\overline{Y}_1\overline{Z}_2}}\right]} \tag{7}$$

Introducing the angular frequency at the resonant condition ω_0, the electrode voltage can be expressed as

$$\overline{V}_e\{\omega_0\} = \frac{\overline{V}_s}{\left[\dfrac{1}{1+\dfrac{1}{\overline{Y}_1\{\omega_0\}\overline{Z}_2\{\omega_0\}}}\right]} \tag{8}$$

where

$$\begin{aligned} \overline{Y}_1 &= j\omega C_1 + \frac{1}{R_1 + j\omega L_1} = \frac{1-\omega^2 C_1 L_1 + j\omega R_1 C_1}{R_1 + j\omega L_1} \\ \overline{Z}_1 &= \frac{R_1 + j\omega L_1}{1-\omega^2 C_1 L_1 + j\omega R_1 C_1} \\ \overline{Z}_2 &= \frac{R_L}{1 + j\omega R_L C_L} \end{aligned} \tag{9}$$

4.2. Calibration

During the calibration stage, the load capacitance C_L was considered as sum of the intrinsic capacitance in the igniter assembly, of the HV probe *Tektronix P6015A* capacitance ($3\ pF\ \pm 2\%$) and of the estimated stray capacitance introduced by the pressure chamber. The calibration was conducted at room temperature and nominal power absorption.

Pressure chamber capacitance assessment

The pressure chamber stray capacitance contributes significantly to the system performance and behaviour. Its calibration was performed on Federal-Mogul Powertrain setup and then estimated by matching the analytic result and the measured resonance frequency (setup shown on section 2.3). The iterative process is based on the frequency resonant criterion (detailed mathematical proof in Appendix):

$$\frac{B\left(\sqrt{C^2+D^2}+C\right)}{D\left(\sqrt{A^2+B^2}+A\right)} = 1 \tag{10}$$

where

$$\begin{aligned} A &= R_1 + R_L - \omega^2 R_L L_1 \left(C_L + C_1\right) \\ B &= \omega \left(L_1 + R_1 R_L \left(C_L + C_1\right)\right) \\ C &= 1 - \omega^2 C_1 \left(R_1 R_L C_L + L_1\right) \\ D &= \omega \left(R_L C_L + R_1 C_1 - \omega^2 C_1 L_1 R_L C_L\right) \end{aligned} \tag{11}$$

Electrode voltage calibration

Since R_1 is the electrical parameter most affected by the operating condition, the model was calibrated basing on experimental data (par. 4.3), by tuning R_1. After the calibration, the analytic model allows to estimate V_e by adjusting the stray capacitance for each setup. The stray capacitance assessment was performed on both FM and UniPG setup.

4.3. Experimental

Fig. 4 shows the measured data of the electrode voltage V_e (black crosses) as a function of the driving voltage V_d, according to the methodology explained in section 3.1. The small dispersion of each of the four

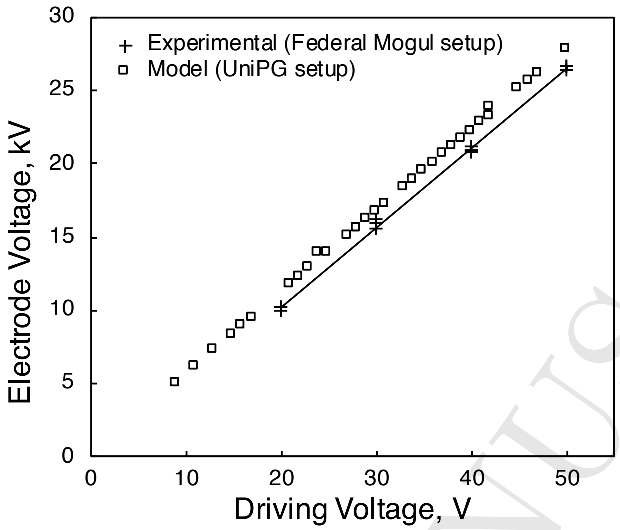

Figure 4: Experimental V_e as a function of V_d, for different T_{on} and p_{ch} (black crosses). The solid line is a linear regression. *FM* electric model of the corona igniter adapted to the *UniPG* test case to predict V_e as a function of V_d for different gas type and p_{ch} (white-filled squares).

data clouds is due to the performance variation between the different igniters used for the test more than to a presumed dependence of V_e on pressure p_{ch} or on discharge duration T_{on}, therefore V_e is constant at fixed V_d. The linear regression (black solid line) highlights the strict linearity of the dependence $V_e = f(V_d)$.

Even if such dependence is clear, it cannot be exported *as it is* to the UniPG data collection. In fact, the experimental tool used to measure the electrode voltage (i.e. the voltage probe) involves a high stray capacitance that affects the data systematically as a bias (gap between crosses and squares in fig. 4). The developed model of the igniter allows to assess the stray capacitance of the measurement system.

5. Experimental results

5.1. Stray Capacitance assessment and Electrode Voltage range

The FM model can be adapted and extended to the UniPG case to calculate V_e, by evaluating the different stray capacitance given by the UniPG system *igniter-pressure sensor*. The measurement of the feeding current frequency of the coil ν_i is required because the stray capacitance affects it (the higher the stray capacitance, the lower the ν_i). This allows to compare its value with the theoretical one and then to derive the estimated stray capacitance. The result shows a current frequency $\nu_i = 1.029\ MHz$ (compared with a theoretical value of 1.04 MHz) therefore the UniPG system is affected by a stray capacitance of about 2.56 pF on average and with a standard deviation of 0.2 pF, rather independent on the applied driving voltage in this range (fig. 5). Therefore, V_e is describable as a linear function of V_d as in fig. 4.

5.2. Corona Duration

This test is led in pure nitrogen starting from the *standard conditions* ($V_d = 40\ V$ and $T_{on} = 300\ \mu s$) by varying the corona duration parameter T_{on}. Between the rise and the fall, the current has a pretty constant behaviour characterised by a different duration consistently with the assigned setup: in fig. 6 is well visible how the subsequent T_{on} increase (fig. 6 *top*, from 100 μs to 500 μs by 100 μs step) implies a wider pressure gradient Δp_{ch} (fig. 6 *bottom*).The corresponding released thermal energy E_r is a linear function of the corona duration T_{on} (fig. 7) in this range of pressure. Therefore, the power supply system and the coil fully support the energy demand and the streamers production rate.

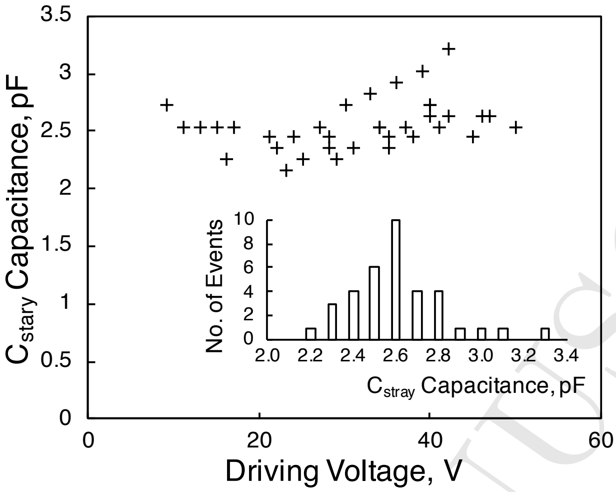

Figure 5: (*Main*) C_{stray} capacitance distribution as a function of V_d. (*Inner*) Occurrence frequency of the same C_{stray} distribution.

Since the energy supplied to the coil E_s is linearly dependent on T_{on}, the efficiency of the igniter η is pretty constant in the range $100-500$ μs, $\eta = 11.8\%$ on average. This value is about an half of the maximum observed (beyond 20%, see section 5.3, fig. 10), due to the selected operating conditions.

5.3. Released energy as a function of the applied electrode voltage

BDV and *CIV* are transition phases where the igniter ACIS emission is characterised by an intrinsically stochastic behaviour. It is possible to define a driving voltage V_d^{CIV}, and consequently an electrode voltage V_e^{CIV}, under which there is no streamer production at all. Similarly, it is possible to define V_d^{BDV}, and so V_e^{BDV}, over which the igniter system works in arc conditions constantly. Both V_d^{BDV} and V_d^{CIV} are functions of the bomb chamber inner pressure p_{ch} and of the filling gas type. For intermediate V_d values (or rather V_e), the igniter generally produces streamers, i.e. the corona effect is active.

On the other hand, when V_d approaches V_d^{CIV} or V_d^{BDV}, the igniter shows the mix of behaviours: succession of corona/failure events (*failure event* is that one with no released energy associated) and corona/spark events, respectively. The more V_d is close to V_d^{CIV}, or V_d^{BDV}, the more is the probability to have null, or spark, events. As a consequence, this aleatory behaviour produces a certain degree of randomness and of arbitrariness in identifying V_d^{BDV} and V_d^{CIV} and, then, in the definition of V_d^0 and V_d^{max}. These are the corresponding operating values for V_d^{BDV} and V_d^{CIV}: the maximum V_d allowed before, respectively, the corona inception and the breakdown. Note that the electronic control system accepts integer values only for V_d (not designed for this fine tuning application). A brief description of the stochastic behaviour of the ACIS system near V_d^{CIV} is given in section 6.2.

Fig. 8 shows the found operating range in terms of electrode voltage V_e, according to the adopted definition of *CIV* and *BDV*, for the different tested pressures p_{ch}. As the definition consequence, the *BDV* points fall on a Paschen curve [73] obtained by a fitting procedure for the specific gap between the electrodes.

Nitrogen

Nitrogen is used as a medium reference case for the pure thermal effect, being almost inert and with a lower radicals production than oxygen [31, 50]. Furthermore, nitrogen is also used for the igniter electrical characterisation by *FM*, allowing a more effective comparison between results.

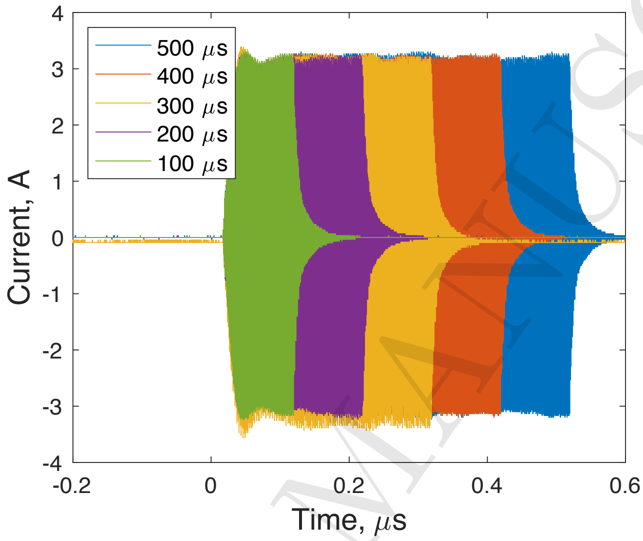

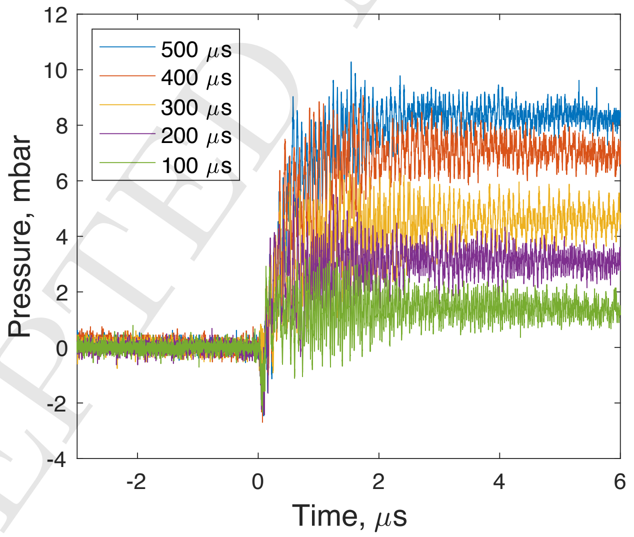

Figure 6: (*Top*) Current produced by the ACIS igniter when the activity duration goes from 100 μs to 500 μs. (*Bottom*) Correspondingly, the measured pressure of the bomb inner chamber increases proportionally.

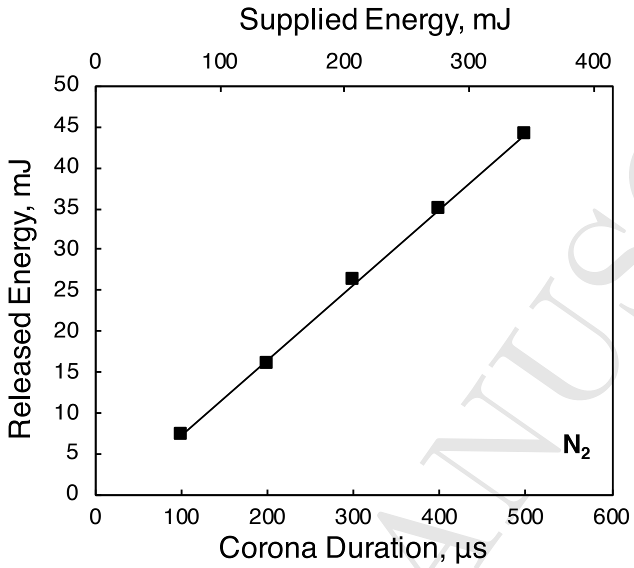

Figure 7: Corona duration test in standard conditions (nitrogen, 5.5 bar, $V_d = 40V$). Each T_{on} corresponds to a certain supplied energy E_s (*top axis*) to the igniter coil. With good approximation, E_r is a linear function of T_{on} (the solid line is a linear regression).

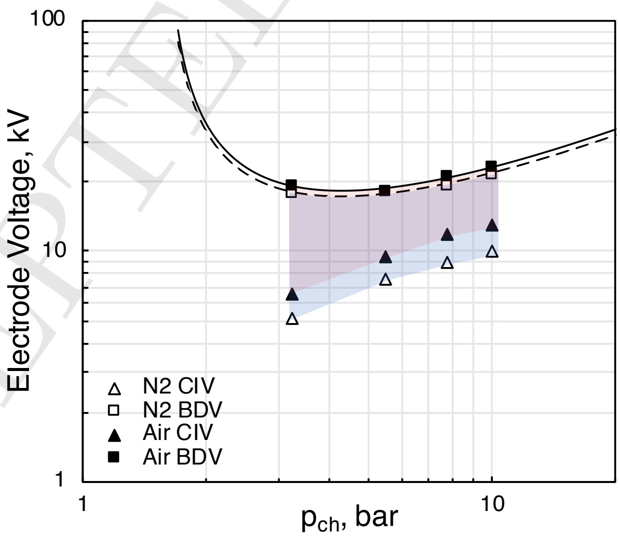

Figure 8: Operating area of the igniter in terms of V_e as a function of p_{ch} (*nitrogen*: transparent blue, white-filled symbols; *air*: transparent red, black-filled symbols). The triangles are the lower limit (*CIV* condition) while the squares specify the upper extremes (*BDV* condition) that fall on the relative Paschen curve (obtained by a fitting procedure, dashed line for nitrogen and solid line for air).

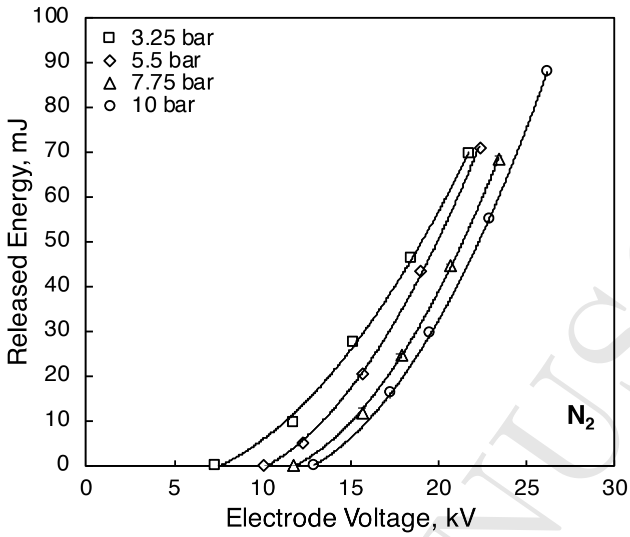

Figure 9: (*Nitrogen*) E_r as a function of V_e for different p_{ch}. The trends are well described by a second order polynomial (solid lines).

The corona inception voltage V_e^{CIV} increases with the applied pressure. Once p_{ch} is set, E_r grows from zero (corresponding to V_d^0 as an increasing function of the electrode potential. The relation can be pretty well described by a second order polynomial (solid lines in fig. 9). Thus, E_r, as a function of V_e, results in a set of parabolas that move towards V_e by increasing p_{ch}. The parabolas bundle seems to be quite tight, gathering towards higher pressure. The maximum of E_r can be found for BDV conditions and, therefore, depends on the Paschen curve of fig. 8. It is about 70 mJ, quite constant, except the 10 bar case (88 mJ).

As a result, higher pressure means lower energy released to the gas medium for the same potential V_e applied to the electrode, in agreement with [31, 74]. This behaviour is the opposite of what seen and expected for the spark case [13, 65], where a pressure increase pushes the released energy and the system efficiency to higher values.

Fig. 10 shows the corresponding efficiency η, defined as in eq. 3, plotted versus E_s. The efficiency quickly increases with V_e from 0% to beyond 20%, independently of p_{ch}, at least four times more than the best efficiency showed by the spark [13, 65]. The starting point and the particular trend instead, are functions of the pressure, according to the behaviour showed in fig. 2 and fig. 9. At 3.25 bar the efficiency highlights a strong decrease of the growth rate. This feature becomes lighter with continuity at higher pressures, where the growth rate is already lower from the beginning. It should be noted that the relative pressure gap between 3.25 bar and 5.5 bar is higher then the one between 7.75 bar and 10 bar, so that, trivially, we should expect bigger changes. Likewise E_r, also the efficiency trend has a fast drop by increasing the pressure, at fixed E_s.

Air

The partial replacement of nitrogen with oxygen changes quantitatively the bunch of curves showed in fig. 9 with no sensitive behaviour twisting (fig. 11): the fast energy fall with the pressure increase and E_r growth with V_e are still well highlighted. Finally, the maximum E_r, just before the breakdown, is quite constant (with the exception of 5.5 bar), included between 70 mJ and 80 mJ: as for the nitrogen case, this trend reflects the impact of the BDV behaviour described by the Paschen curve. On the other hand, compared to the nitrogen case, the bunch is not so tight. Furthermore, the curves move to higher V_e almost linearly with the increase of p_{ch} starting from the *zero-point* (that reflects the CIV trend of fig. 8). These differences seem to widen at high pressure.

The bunch broadening and the higher requested potential for the CIV are probably due to the quenching effect of the oxygen component of the air, as observed in [75]: since the oxygen easily captures a fraction

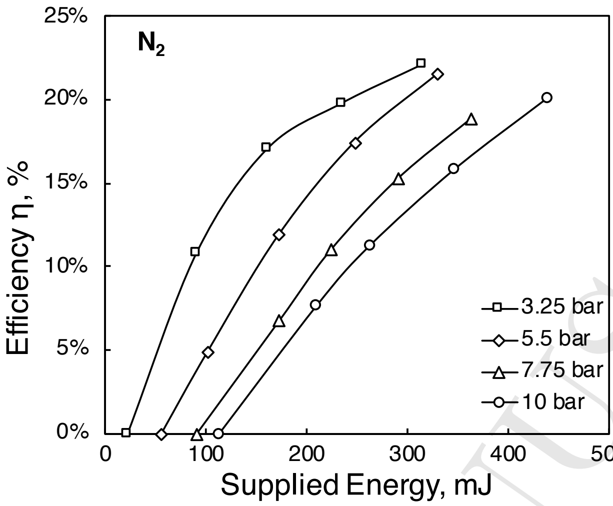

Figure 10: (*Nitrogen*) Efficiency η of the corona igniter as a function of the coil E_s, for different p_{ch}. The solid lines are drawn only for sake of plot legibility.

of the emitted electrons, it limits and prevents the corona effect occurrence. The wide multiplicity of the produced oxygen states, molecular or atomic ionised, excited and metastable states [76], generates a variety of different available channels to degrade the energy absorbed by the chamber medium. Not all the energy referred to these channels is, finally, measurable as thermal energy.

Furthermore, the oxygen presence highlights a feature that the nitrogen case just hinted: the theoretical possibility of having an intersection between consecutive curves (in particular, the 3.25 *bar* and the 5.5 *bar* curves). This would mean a radically new, opposite, behaviour: after the crossing of the curves, E_r would increases with the pressure instead of decreasing (see deeper analysis in sec. 6). The high voltage zone, here not reachable because of the arc onset, could be explored in future work in different operating conditions to experimentally confirm this supposed inversion.

The igniter efficiency η confirms what seen in the nitrogen case, stressing some features as the tendency to sharply increase to reach a plateau, clear at 3.25 *bar* while more indefinite at higher pressure (fig. 12). The efficiency reaches its maximum value around 20% at the lower pressure (3.25 *bar*) for the higher electrode potential available. Anyway, at the applied operating conditions with air, the efficiency is generally lower than the nitrogen case since it needs higher value of the E_s to release a comparable amount of thermal energy.

Generally, the air data suffers of a larger uncertainty (compare fig. 10 and 12): this could be related to the aggressive byproducts of the oxygen chemistry that affect somehow the performances, increasing the measurement dispersion.

6. Discussion

The collected data establish some evidences here summarised:

- the electrode voltage is linearly proportional to the driving voltage ($V_e \propto V_d$);
- the released energy, at fixed chamber pressure and driving voltage, is linearly proportional to the streamers time of activity, the *corona duration* ($E_r \propto T_{on}$);
- E_r, at fixed p_{ch} and V_d, is experimentally proportional to the square of the driving voltage ($E_r \propto V_d^2$) and thus to the square of the electrode voltage ($E_r \propto V_e^2$);
- the same E_r drops quickly by increasing p_{ch}, at fixed V_d;

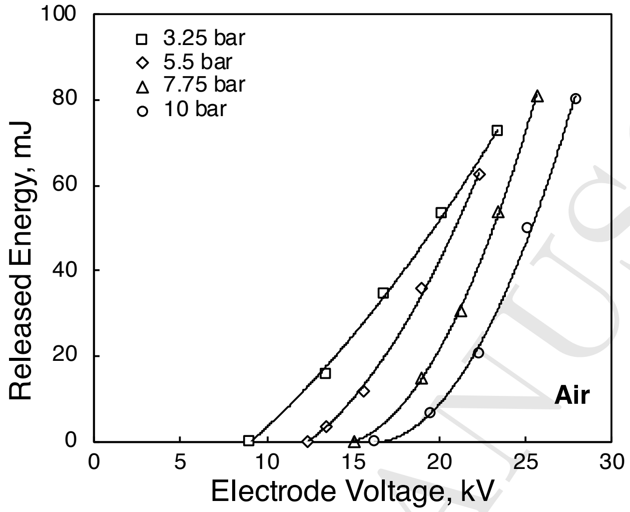

Figure 11: (Air) E_r as a function of V_e for different p_{ch}. Also for the air case, the trends are well described by a second order polynomial (solid lines).

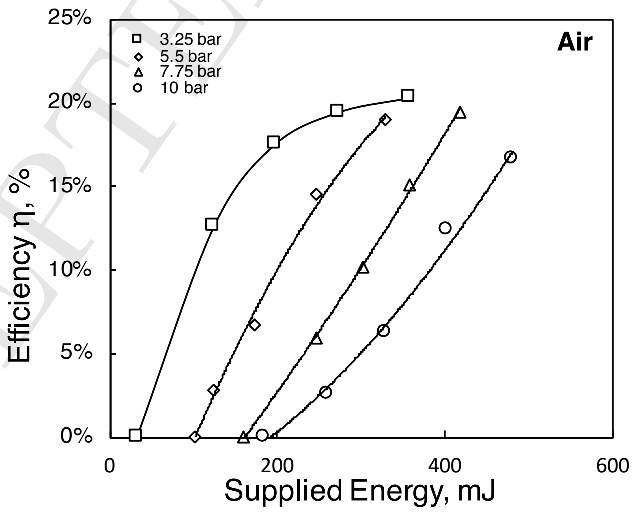

Figure 12: (Air) Efficiency η of the corona igniter as a function of the coil E_s for different p_{ch}. The solid lines are drawn only for sake of plot legibility.

- it is expected that the trend is reversed at high V_e and low p_{ch}.

Generally speaking, V_e establishes on the bomb chamber medium an electric field that, by means of intermediate stochastic processes as ionisation or photo-ionisation, produces free electrons and accelerates them, activating the avalanche production mechanism [35, 67]. Once electrons and positive ions are created, the latter move towards the negative electrode with a drift velocity v^{ion}_{drift}. For low ratio between the electric field $\mathbf{E}$ and the pressure p_{ch} (i.e. the *reduced electric field* $\mathbf{E}/p_{ch}$, or more accurately $\mathbf{E}/N$, where N is the gas particle concentration, proportional to the medium density), v^{ion}_{drift} is proportional to the reduced electric field:

$$v^{ion}_{drift} \propto \frac{\mathbf{E}}{p_{ch}}\,, \qquad (low \quad \mathbf{E}/p_{ch}) \tag{12}$$

For high values of the ratio $\mathbf{E}/p_{ch}$, the ions drift velocity is proportional to the square root of the reduced electric field [66]:

$$v^{ion}_{drift} \propto \sqrt{\frac{\mathbf{E}}{p_{ch}}}\,, \qquad (high \quad \mathbf{E}/p_{ch}) \tag{13}$$

The drift velocity is the main ionic velocity component, once averaged. Ions' kinetic energy, proportional to the square of the gained drift velocity, is then transferred to the medium during the thermalization process. Therefore, the experimental data imply a linear dependence between the electrode voltage and the ions drift velocity. Intuitively, it can be assumed that the dependence described by eq. 13 could affect the lower pressure test (3.25 *bar*) at higher electrode voltage ($10 - 15\ kV$), recognisable in a linear trend (in particular for the air case). Of course, this hypothesis should be conveniently verified.

Electron drift velocity v^{el}_{drift} follows as well a relation similar to eq. 13 at ionising energies [66]:

$$v^{el}_{drift} \propto \sqrt{\frac{\mathbf{E}}{p_{ch}}} \tag{14}$$

Since the curves of fig. 9 and 11 do not show linear behaviour, we should conclude that the electrons contribution to the thermal energy is lower than the ions' one as long as the eq. 12 is true. Furthermore, not the whole electron kinetic energy is degraded into thermal energy since it is also employed in radicals production and photons emission.

6.1. Released Energy Parametrization

This kind of considerations let us expect the behaviour showed in fig. 9-11 and, therefore, it allows to use a second order polynomial as a model, according to the expression

$$E_r = aV_e^2 + bV_e + c \tag{15}$$

and to find the best fitting curves (namely, a, b and c) to represent the collected data.

Fig. 13 (*top*) compares the trends of the a coefficients for nitrogen (a^{N_2}) and air (a^{Air}). The a coefficient is an estimator of how quickly E_r grows with V_e. Both trends increase until the coefficients reach a plateau at high pressure values. The nitrogen case (*dashed line*) is much more stable and the growth is small. The air coefficient a^{Air} starts from a lower value, compared to a^{N_2}, and quickly increases. Probably, this is due to the availability of higher V_e ($V_e^{BDV}|_{air}$ is higher than $V_e^{BDV}|_{N_2}$ see fig. 8), corresponding to higher E_s (and power). a^{Air} tends towards very low values at low p_{ch}. Consequently, the relation $E_r = E_r(V_e)$ approaches a transition to a linear behaviour.

The coefficients b and c are less meaningful, even if both monotonic: they contribute with a to determine $V_e|_{E_r=0}$, the electrode tension value such that E_r is null, i.e. the abscissa intercept. The latter corresponds to the experimental value found for V_e^{CIV} and therefore shows analogous monotonic increasing trend.

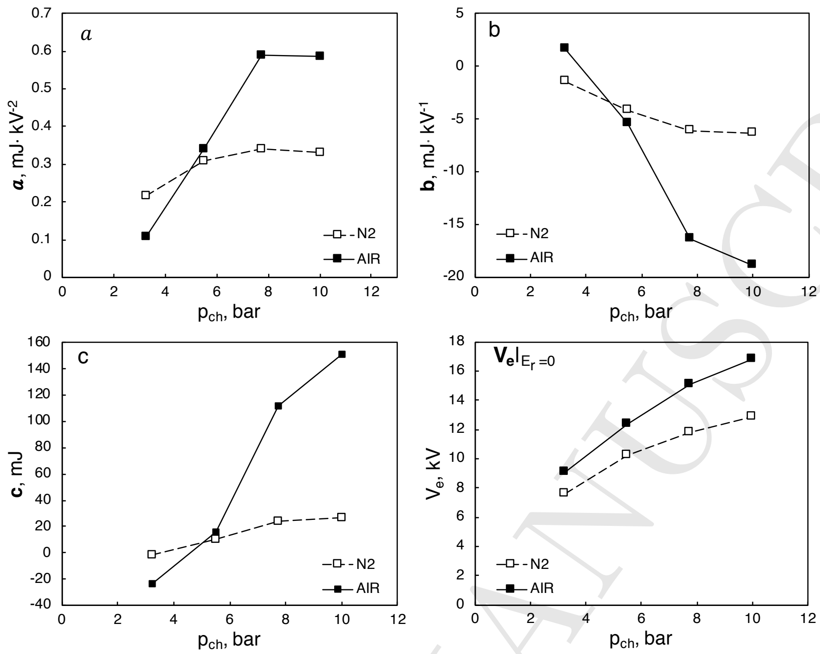

Figure 13: Trend of the second order polynomial coefficients as a function of p_{ch} for the nitrogen (*dashed line*) and air (*solid line*) cases, according to the expression $E_r = aV_e^2 + bV_e + c$. (*Bottom right*) Trend of the abscissa intercept $V_e|_{E_r=0}$ (the tension value such that E_r is *zero*) of the same function, corresponding to V_e^{CIV}.

The description of $E_r = E_r(V_e)$, via a second order polynomial, allows to build a map of the released energy as a function of p_{ch} (fig. 14) for arbitrary values (in the tested range) of E_s, thanks to the parametrization showed in fig. 2.

The map is built by linearly increasing E_s (evenly spaced steps of $\Delta E_s = 26.8\ mJ$ for both gases) from 105.2 mJ to 346.4 mJ for the nitrogen (dotted lines) and from 105.2 mJ to 373.2 mJ for the Air case (solid lines). E_s increases according to the black arrow in fig. 14, where only the two highest E_s levels are pointed out (for both gases). The released energy behaviour showed in the map is not trivial. The iso-energy curves E_s establish a tight bundle for low and high pressure while it is wide in the middle range of p_{ch}. This happens for both pure nitrogen and air. A tight bundle means that a lot of E_s is needed to reach relatively high value of E_r. This is particularly true for air at highest pressure and it is related to the igniter difficulty to quickly reach high efficiency in such operating conditions (fig. 12). Nitrogen is much more stable, with no dramatic fall at high pressure.

The area around 5.5 *bar* in fig. 14 is of a certain interest, since the density reduction of the iso-energy curves denotes an easier condition to reach high efficiency. In addition, for the air case this area is featured with a maximum for the highest iso-energy curves. The remaining ones, instead, are monotonic decreasing. The decreasing trend with p_{ch} is the typical behaviour observed in fig. 11. A maximum means that the released energy, locally, does not depend on the chamber pressure. As a consequence, there is an $E_r = E_r(p_{ch})$ trend transition from decreasing (at higher pressure) to increasing (at lower pressure): a real behaviour inversion. The local maximum of fig. 14 is related to the intersection, experimentally *still not reached*, in fig. 11 between the 3.25 *bar* and 5.5 *bar* curves at the higher value of V_e.

Such inversion is only inferred since the breakdown occurs and prevents to achieve the corresponding operating conditions. On the other hand, the breakdown is due only to the geometrical features of inner chamber (gap between the electrodes). The monotonic trends of the polynomial coefficients (fig. 13) imply that the curves intersection eventually occurs.

Under this assumption, at higher V_e, i.e. at higher free electron energy, a pressure increase, that means

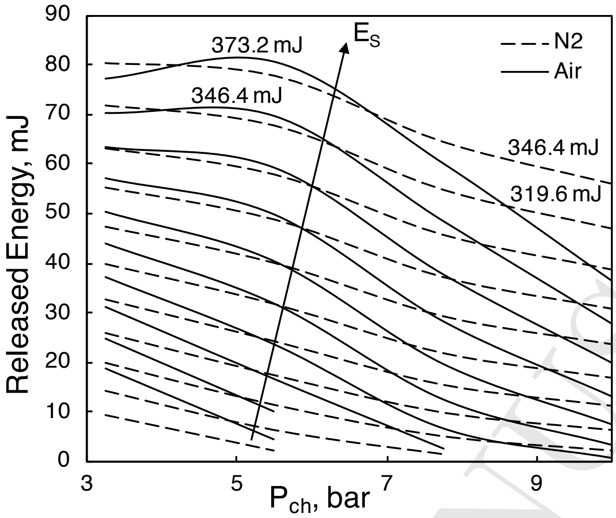

Figure 14: Map of the inferred trend of the released energy E_r to the bomb chamber medium as a function of the inner pressure p_{ch} and for various level of energy supplied to the coil E_s, for both tested gas types, nitrogen (*dotted lines*) and air (*solid lines*).

a particle density increment and a mean free path decrease, would produce:

- a growth of the scattering occurrences;
- an improvement of the energy transfer efficiency in the medium.

Anyway, the change of behaviour at low pressure is not completely unexpected since many variables affect the system. For example, the low pressure supports the atomic oxygen excited state production [31]. As already reported in the introduction, this is an efficient channel to heat the gas: E_r differences between air and nitrogen are smaller at the lowest pressure, where the maximum of fig. 14 takes place. Furthermore, we already saw that the ions' kinetic energy is heavily affected from the $\mathbf{E}/p_{ch}$ ratio and therefore the trend change may suggest a slow transition from the eq. 12 regime description towards the eq. 13 one, by lowering p_{ch}. Finally, high pressure produces a change in the streamer propagation [31] due to a change in the ionisation-recombination balance [77] and in mechanisms as photoionisation by the excited-state quenching of molecular nitrogen [78].

6.2. Stochastic Behaviour Description

The nitrogen 7.75 *bar* data explain the typical stochastic behaviour of the Corona effect just over the *CIV* condition. To each V_e corresponds a series of raw measurements of E_r versus time, each one characterised by a small dispersion (fig. 15). On the contrary, the 12 kV series (black cross) shows a particularly fluctuating trend, with many *zeros* too. This data collection can be gathered as in the histogram of fig. 16 (*white-filled bars*) where it is easy to distinguish five different energy values around which the data are concentrated. Therefore, we can rearrange consequently the histogram with just five groups as in fig. 16 (*black-filled bars*) and find the corresponding five energy levels (included the 0 mJ level). The energy of each group is simply defined as the energy average of the corona events belonging to the same group.

Fig. 17 reports the five energy levels relative to the 12 kV series compared to the whole sequence of 7.75 *bar* data collection, included the corresponding fitting curve. The series is distributed from 0 mJ up to the fitting curve, that corresponds to the higher energy level (~ 9.9 mJ). This unpredictable behaviour was clarified by a previous test led on the optical engine and reported in [56]: indeed, approaching the V_e^{CIV}

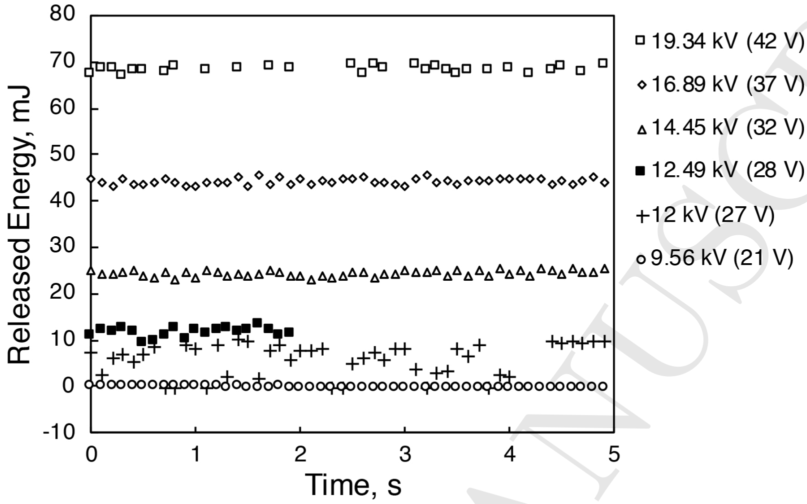

Figure 15: Nitrogen case at $p_{ch} = 7.75\ bar$, E_r distributions corresponding to the various level of V_e, whole data series. The distribution of 12 kV data series is distinctly the widest.

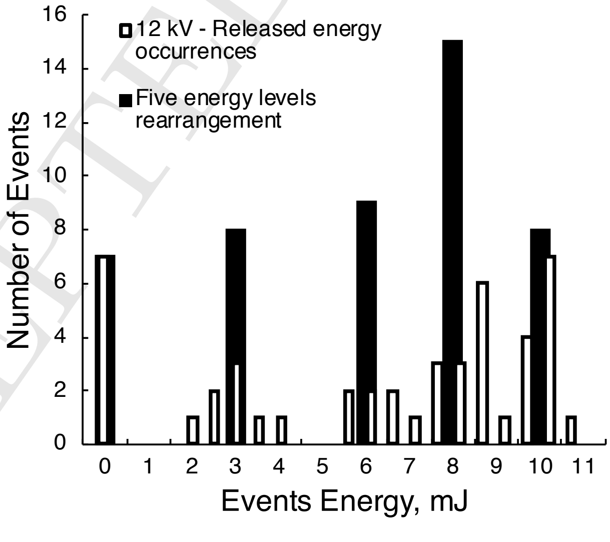

Figure 16: Nitrogen case at $p_{ch} = 7.75\ bar$, detail of the 12 kV data series. The E_r distribution of the occurred events (*white-filled bars*) suggests a regular structure attributable to different igniter emission modes. The distribution can be correspondingly rearranged according to the assumption of an emission characterised by a different number of streamers (*black-filled bars*).

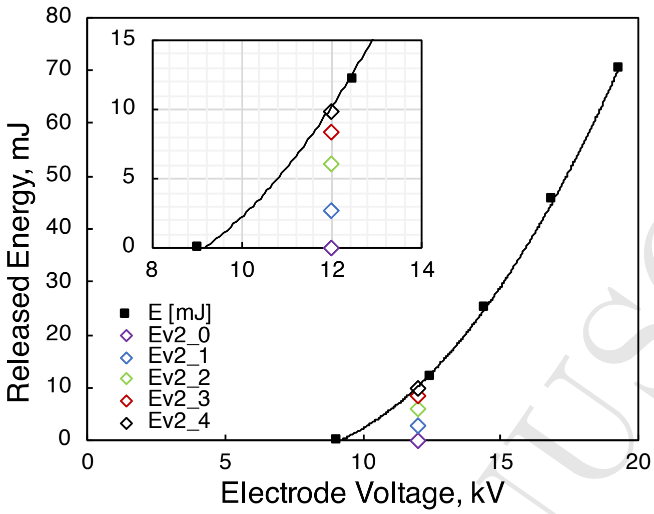

Figure 17: E_r distribution of the nitrogen *sub*-cases at $V_e = 12\ kV$, compared to the whole tested sequence of 7.75 bar. The sub-plot contains a zoom of the area including the 12 kV points.

conditions from higher voltage, V_e is not high enough to generate all the four standard streamers for every shot, so we can obtain from four to no streamers at all for each shot. As observed, the behaviour is strongly stochastic and suggests that, under a certain threshold of V_e and above V_e^{CIV}, the production of a particular number of streamers has its own probability, depending on how close V_e is to V_e^{CIV}.

7. Conclusions

In this work, we tested a radio-frequency igniter based on the corona effect (ACIS) to have a systematic characterisation of the thermal energy released by the igniter in a constant volume vessel both in pure nitrogen and pure air. The inner pressure of the vessel, the type of medium (nitrogen or air) and the operating parameters of the igniter (driving voltage and the corona discharge duration) are all settable and matter of analysis.

We can summarise the main results as follow:

- A lumped-parameter circuit model of the igniter was developed and calibrated with experimental data to determine the stray capacitance of the calorimeter and to foresee the electrode voltage of the igniter, depending on the control parameters.

- The thermal energy released to the medium from the igniter is linearly proportional to the duration of the corona discharge.

- The thermal energy released to the medium grows proportionally to the square of the electrode voltage (or, operatively, of the driving voltage).

- In general, higher pressures of the medium need higher electrode voltage values to release the same amount of thermal energy.

- Air, as vessel medium, brings a lower value of thermal energy released compared to nitrogen in similar operating conditions. It is worth noticing that air is much more aggressive towards the electrode and needs special care to guarantee a reliable measurement process.

- Both in nitrogen and air, the igniter is able to reach more than 20% of efficiency.

- A map of the thermal energy released, as a function of the medium pressure and of the electrode voltage, was produced for both nitrogen and air. The behaviour is not trivial and, in particular operating conditions, shows a maximum that produces an inversion of the dependence between thermal energy and pressure.
- The behaviour of the igniter becomes stochastic when the electrode voltage values approaches the corona inception voltage. This is due to the lost capability to constantly generate the default four corona streamers for each corona shot.

References

[1] Wei, H., Zhu, T., Shu, G., Tan, L., Wang, Y.. Gasoline engine exhaust gas recirculation – A review. Applied Energy 2012;99(X):534–544. URL: `http://dx.doi.org/10.1016/j.apenergy.2012.05.011https://linkinghub.elsevier.com/retrieve/pii/S0306261912003595`. doi:`10.1016/j.apenergy.2012.05.011`.

[2] Kim, K., Kim, J., Oh, S., Kim, C., Lee, Y.. Evaluation of injection and ignition schemes for the ultra-lean combustion direct-injection LPG engine to control particulate emissions. Applied Energy 2017;194:123–135. URL: `http://dx.doi.org/10.1016/j.apenergy.2017.03.012https://linkinghub.elsevier.com/retrieve/pii/S0306261917302271`. doi:`10.1016/j.apenergy.2017.03.012`.

[3] Jung, D., Sasaki, K., Iida, N.. Effects of increased spark discharge energy and enhanced in-cylinder turbulence level on lean limits and cycle-to-cycle variations of combustion for SI engine operation. Applied Energy 2017;205(August):1467–1477. URL: `http://dx.doi.org/10.1016/j.apenergy.2017.08.043https://linkinghub.elsevier.com/retrieve/pii/S0306261917310590`. doi:`10.1016/j.apenergy.2017.08.043`.

[4] Hayashi, N., Sugiura, A., Abe, Y., Suzuki, K.. Development of Ignition Technology for Dilute Combustion Engines. SAE International Journal of Engines 2017;10(3):2017–01–0676. URL: `https://www.sae.org/content/2017-01-0676/`. doi:`10.4271/2017-01-0676`.

[5] Takahashi, E., Kojima, H., Furutani, H.. Advanced ignition technology for the achievement of high thermal efficiency of internal combustion engine. Synthesiology English edition 2015;8(4):187–195. URL: `https://www.jstage.jst.go.jp/article/syntheng/8/4/8{_}187/{_}article`. doi:`10.5571/syntheng.8.4_187`.

[6] Hoppe, F., Thewes, M., Baumgarten, H., Dohmen, J.. Water injection for gasoline engines: Potentials, challenges, and solutions. International Journal of Engine Research 2016;17(1):86–96. URL: `http://journals.sagepub.com/doi/10.1177/1468087415599867`. doi:`10.1177/1468087415599867`.

[7] Hoppe, F., Thewes, M., Seibel, J., Balazs, A., Scharf, J.. Evaluation of the Potential of Water Injection for Gasoline Engines. SAE International Journal of Engines 2017;10(5):2017–24–0149. URL: `https://www.sae.org/content/2017-24-0149/`. doi:`10.4271/2017-24-0149`.

[8] Bozza, F., De Bellis, V., Teodosio, L.. Potentials of cooled EGR and water injection for knock resistance and fuel consumption improvements of gasoline engines. Applied Energy 2016;169:112–125. URL: `http://dx.doi.org/10.1016/j.apenergy.2016.01.129https://linkinghub.elsevier.com/retrieve/pii/S0306261916301179`. doi:`10.1016/j.apenergy.2016.01.129`.

[9] Worm, J., Naber, J., Duncan, J., Barros, S., Atkinson, W.. Water Injection as an Enabler for Increased Efficiency at High-Load in a Direct Injected, Boosted, SI Engine. SAE International Journal of Engines 2017;10(3):2017–01–0663. URL: `https://www.sae.org/content/2017-01-0663/`. doi:`10.4271/2017-01-0663`.

[10] Battistoni, M., Grimaldi, C.N., Cruccolini, V., Discepoli, G., De Cesare, M.. Assessment of Port Water Injection Strategies to Control Knock in a GDI Engine through Multi-Cycle CFD Simulations. In: SAE Technical Paper. 2017,URL: `http://papers.sae.org/2017-24-0034/`. doi:`10.4271/2017-24-0034`.

[11] Dale, J.D., Checkel, M.D., Smy, P.R.. Application of high energy ignition systems to engines. Progress in Energy and Combustion Science 1997;23(5-6):379–398. URL: `https://linkinghub.elsevier.com/retrieve/pii/S0360128597000117`. doi:`10.1016/S0360-1285(97)00011-7`.

[12] Kawahara, N., Hashimoto, S., Tomita, E.. Spark discharge ignition process in a spark-ignition engine using a time series of spectra measurements. Proceedings of the Combustion Institute 2017;36(3):3451–3458. URL: `https://linkinghub.elsevier.com/retrieve/pii/S1540748916304187`. doi:`10.1016/j.proci.2016.08.029`.

[13] Abidin, Z., Chadwell, C.. Parametric Study and Secondary Circuit Model Calibration Using Spark Calorimeter Testing. In: SAE Paper. 2015,URL: `http://papers.sae.org/2015-01-0778/`. doi:`10.4271/2015-01-0778`.

[14] Ran, Z., Hariharan, D., Lawler, B., Mamalis, S.. Experimental study of lean spark ignition combustion using gasoline, ethanol, natural gas, and syngas. Fuel 2019;235(May 2018):530–537. URL: `https://doi.org/10.1016/j.fuel.2018.08.054https://linkinghub.elsevier.com/retrieve/pii/S001623611831425X`. doi:`10.1016/j.fuel.2018.08.054`.

[15] Jiang, L.J., Shy, S.S., Nguyen, M.T., Huang, S.Y., Yu, D.W.. Spark ignition probability and minimum ignition energy transition of the lean iso-octane/air mixture in premixed turbulent combustion. Combustion and Flame 2018;187:87–95. URL: `https://doi.org/10.1016/j.combustflame.2017.09.006https://linkinghub.elsevier.com/retrieve/pii/S001021801730336X`. doi:`10.1016/j.combustflame.2017.09.006`.

[16] Turquand d'Auzay, C., Papapostolou, V., Ahmed, S.F., Chakraborty, N.. On the minimum ignition energy and its transition in the localised forced ignition of turbulent homogeneous mixtures. Combustion and Flame 2019;201:104–117. URL: `https://linkinghub.elsevier.com/retrieve/pii/S0010218018305327`. doi:`10.1016/j.combustflame.2018.12.015`.

[17] Jung, D., Iida, N.. An investigation of multiple spark discharge using multi-coil ignition system for improving thermal efficiency of lean SI engine operation. Applied Energy 2018;212(December 2017):322–332. URL: `https://doi.org/10.1016/j.apenergy.2017.12.032https://linkinghub.elsevier.com/retrieve/pii/S0306261917317476`. doi:`10.1016/j.apenergy.2017.12.032`.

[18] Tsuboi, S., Miyokawa, S., Matsuda, M., Yokomori, T., Iida, N.. Influence of spark discharge characteristics on ignition and combustion process and the lean operation limit in a spark ignition engine. Applied Energy 2019;250(May):617–632. URL: `https://doi.org/10.1016/j.apenergy.2019.05.036https://linkinghub.elsevier.com/retrieve/pii/S0306261919308906`. doi:`10.1016/j.apenergy.2019.05.036`.

[19] Yu, X., Yu, S., Yang, Z., Tan, Q., Ives, M., Li, L., et al. Improvement on Energy Efficiency of the Spark Ignition System. In: SAE Technical Paper Series; vol. 1. 2017,URL: `https://www.sae.org/content/2017-01-0678/`. doi:`10.4271/2017-01-0678`.

[20] Soldera, F., Lasagni, A., Mücklich, F., Kaiser, T., Hrastnik, K.. Determination of the cathode erosion and temperature for the phases of high voltage discharges using FEM simulations. Computational Materials Science 2005;32(1):123–139. URL: `https://linkinghub.elsevier.com/retrieve/pii/S0927025604001806`. doi:`10.1016/j.commatsci.2004.06.004`.

[21] Lasagni, A., Soldera, F., Mücklich, F.. FEM simulation of local heating and melting during electrical discharge plasma impact. Modelling and Simulation in Materials Science and Engineering 2004;12(5):835–844. URL: `http://stacks.iop.org/0965-0393/12/i=5/a=005?key=crossref.87bccbf9266f72080e0f108190111df9`. doi:`10.1088/0965-0393/12/5/005`.

[22] Breden, D., Karpatne, A., Suzuki, K., Raja, L.. High-Fidelity Numerical Modeling of Spark Plug Erosion. In: SAE Technical Papers; vol. 2019-April. 2019, p. 1–12. URL: `https://www.sae.org/content/2019-01-0215/`. doi:`10.4271/2019-01-0215`.

[23] Badawy, T., Bao, X., Xu, H.. Impact of spark plug gap on flame kernel propagation and engine performance. Applied Energy 2017;191:311–327. URL: `http://dx.doi.org/10.1016/j.apenergy.2017.01.059https://linkinghub.elsevier.com/retrieve/pii/S0306261917300673`. doi:`10.1016/j.apenergy.2017.01.059`.

[24] Ghaderi Masouleh, M., Keskinen, K., Kaario, O., Kahila, H., Wright, Y., Vuorinen, V.. Flow and thermal field effects on cycle-to-cycle variation of combustion: scale-resolving simulation in a spark ignited simplified engine configuration. Applied Energy 2018;230(May):486–505. URL: `https://linkinghub.elsevier.com/retrieve/pii/S0306261918312017`. doi:`10.1016/j.apenergy.2018.08.046`.

[25] Ghaderi Masouleh, M., Keskinen, K., Kaario, O., Kahila, H., Karimkashi, S., Vuorinen, V.. Modeling cycle-to-cycle variations in spark ignited combustion engines by scale-resolving simulations for different engine speeds. Applied Energy 2019;250(May):801–820. URL: `https://doi.org/10.1016/j.apenergy.2019.03.198https://linkinghub.elsevier.com/retrieve/pii/S0306261919306142`. doi:`10.1016/j.apenergy.2019.03.198`.

[26] Lo, A., Cessou, A., Lacour, C., Lecordier, B., Boubert, P., Xu, D.A., et al. Streamer-to-spark transition initiated by a nanosecond overvoltage pulsed discharge in air. Plasma Sources Science and Technology 2017;26(4):045012. URL: `http://stacks.iop.org/0963-0252/26/i=4/a=045012?key=crossref.81db59bd6ccc4b415826855c013e767d`. doi:`10.1088/1361-6595/aa5c78`.

[27] Starikovskii, A.. Plasma supported combustion. Proceedings of the Combustion Institute 2005;30(2):2405–2417. URL: `http://dx.doi.org/10.1016/j.proci.2004.08.272https://linkinghub.elsevier.com/retrieve/pii/S0082078404003285`. doi:`10.1016/j.proci.2004.08.272`.

[28] Shcherbanev, S., De Martino, A., Khomenko, A., Starikovskaia, S.M., Padala, S., Ikeda, Y.. Emission Spectroscopy Study of the Microwave Discharge Igniter. 2017, p. 1–7. URL: `http://papers.sae.org/2017-24-0153/`. doi:`10.4271/2017-24-0153`.

[29] Huang, S., Li, T., Zhang, Z., Ma, P.. Rotational and vibrational temperatures in the spark plasma by various discharge energies and strategies. Applied Energy 2019;251(April):113358. URL: `https://doi.org/10.1016/j.apenergy.2019.113358https://linkinghub.elsevier.com/retrieve/pii/S0306261919310323`. doi:`10.1016/j.apenergy.2019.113358`.

[30] Popov, N.A.. Kinetic processes initiated by a nanosecond high-current discharge in hot air. Plasma Physics Reports 2011;37(9):807–815. URL: `http://link.springer.com/10.1134/S1063780X1108006X`. doi:`10.1134/S1063780X1108006X`.

[31] Wolk, B.M., Ekoto, I.. Calorimetry and Imaging of Plasma Produced by a Pulsed Nanosecond Discharge Igniter in EGR Gases at Engine-Relevant Densities. SAE International Journal of Engines 2017;10(3):2017–01–0674. URL: `http://papers.sae.org/2017-01-0674/`. doi:`10.4271/2017-01-0674`.

[32] Shiraishi, T., Urushihara, T.. Fundamental Analysis of Combustion Initiation Characteristics of Low Temperature Plasma Ignition for Internal Combustion Gasoline Engine. 2011,URL: `http://papers.sae.org/2011-01-0660/`. doi:`10.4271/2011-01-0660`.

[33] Ono, R., Oda, T.. Formation and structure of primary and secondary streamers in positive pulsed corona discharge—effect of oxygen concentration and applied voltage. Journal of Physics D: Applied Physics 2003;36(16):1952–1958. URL: `http://stacks.iop.org/0022-3727/36/i=16/a=306?key=crossref.353589ee29d2d6e034d78fd143a766d2`. doi:`10.1088/0022-3727/36/16/306`.

[34] Hwang, J., Bae, C., Park, J., Choe, W., Cha, J., Woo, S.. Microwave-assisted plasma ignition in a constant volume combustion chamber. Combustion and Flame 2016;167:86–96. URL: `http://dx.doi.org/10.1016/j.combustflame.2016.02.023https://linkinghub.elsevier.com/retrieve/pii/S0010218016000791`. doi:`10.1016/j.combustflame.2016.02.023`.

[35] Kuffel, E., Kuffel, P., Zaengl, W., Zaengl, W., Kuffel, J.. High Voltage Engineering Fundamentals. Applied Electricity and Electronics; Elsevier Science; 2000. ISBN 9780750636346. URL: `https://books.google.it/books?id=jDn78ePM-nwC`.

[36] Padala, S., Le, M.K., Wachi, Y., Ikeda, Y.. Effects of Microwave Enhanced Plasma on Diesel Spray Combustion. SAE Technical Paper Series 2017;1(x):2–8. URL: `https://www.sae.org/content/2017-01-0707/`. doi:`10.4271/2017-01-0707`.

[37] Wu, L., Lane, J., Cernansky, N., Miller, D., Fridman, A., Starikovskiy, A.. Plasma-assisted ignition below self-ignition threshold in methane, ethane, propane and butane-air mixtures. Proceedings of the Combustion Institute 2011;33(2):3219–

3224. URL: https://linkinghub.elsevier.com/retrieve/pii/S1540748910000064. doi:10.1016/j.proci.2010.06.003.

[38] Starikovskaia, S.M.. Plasma assisted ignition and combustion. Journal of Physics D: Applied Physics 2006;39(16):R265–R299. URL: http://stacks.iop.org/0022-3727/39/R265http://stacks.iop.org/0022-3727/39/i=16/a=R01?key=crossref.978ad5eef7e6c1e79038889cadc11150. doi:10.1088/0022-3727/39/16/R01.

[39] Adamovich, I.V., Choi, I., Jiang, N., Kim, J.H., Keshav, S., Lempert, W.R., et al. Plasma assisted ignition and high-speed flow control: non-thermal and thermal effects. Plasma Sources Science and Technology 2009;18(3):034018. URL: http://stacks.iop.org/0963-0252/18/i=3/a=034018?key=crossref.7505a9d74bdf89f850a532d4d00bbc3e. doi:10.1088/0963-0252/18/3/034018.

[40] Mariani, A., Foucher, F.. Radio frequency spark plug: An ignition system for modern internal combustion engines. Applied Energy 2014;122:151–161. URL: http://dx.doi.org/10.1016/j.apenergy.2014.02.009http://linkinghub.elsevier.com/retrieve/pii/S0306261914001287. doi:10.1016/j.apenergy.2014.02.009.

[41] Ju, Y., Sun, W.. Plasma assisted combustion: Dynamics and chemistry. Progress in Energy and Combustion Science 2015;48(C):21–83. URL: http://dx.doi.org/10.1016/j.pecs.2014.12.002http://linkinghub.elsevier.com/retrieve/pii/S0360128514000781https://linkinghub.elsevier.com/retrieve/pii/S0360128514000781. doi:10.1016/j.pecs.2014.12.002.

[42] Hahn, J., Schenk, M., Schauer, F.X., Sauer, C., Weber, G., Schwarz, C.. From glow tube to corona – challenges to the ignition systems of future SI engines. x. ISBN 978-3-658-17108-7; 2017, p. 123–145. URL: http://link.springer.com/10.1007/978-3-658-17109-4http://link.springer.com/10.1007/978-3-658-17109-4{_}9. doi:10.1007/978-3-658-17109-4_9.

[43] Singleton, D., Pendleton, S.J., Gundersen, M.A.. The role of non-thermal transient plasma for enhanced flame ignition in C2H4-air. Journal of Physics D: Applied Physics 2011;44(2):022001. URL: http://stacks.iop.org/0022-3727/44/i=2/a=022001?key=crossref.7f71843701e9c11aedbdb4be72cb9047. doi:10.1088/0022-3727/44/2/022001.

[44] Idicheria, C.A., Najt, P.M.. Potential of Advanced Corona Ignition System (ACIS) for Future Engine Applications. In: Ignition Systems for Gasoline Engines. Cham: Springer International Publishing. ISBN 978-3-319-45503-7; 2017, p. 315–331. URL: http://link.springer.com/10.1007/978-3-319-45504-4{_}19. doi:10.1007/978-3-319-45504-4_19.

[45] Hwang, J., Kim, W., Bae, C., Choe, W., Cha, J., Woo, S.. Application of a novel microwave-assisted plasma ignition system in a direct injection gasoline engine. Applied Energy 2017;205(April):562–576. URL: http://dx.doi.org/10.1016/j.apenergy.2017.07.129https://linkinghub.elsevier.com/retrieve/pii/S0306261917310012. doi:10.1016/j.apenergy.2017.07.129.

[46] Ju, Y., Sun, W.. Plasma assisted combustion: Progress, challenges, and opportunities. Combustion and Flame 2015;162(3):529–532. URL: http://dx.doi.org/10.1016/j.combustflame.2015.01.017https://linkinghub.elsevier.com/retrieve/pii/S0010218015000280. doi:10.1016/j.combustflame.2015.01.017.

[47] Luque, A., Ratushnaya, V., Ebert, U.. Positive and negative streamers in ambient air: modelling evolution and velocities. Journal of Physics D: Applied Physics 2008;41(23):234005. URL: http://stacks.iop.org/0022-3727/41/i=23/a=234005?key=crossref.b6c5e6259f2a7c9b1cddeb7a6690262c. doi:10.1088/0022-3727/41/23/234005.

[48] Breden, D., Idicheria, C.A., Keum, S., Najt, P.M., Raja, L.L.. Modeling of a Dielectric-Barrier Discharge-Based Cold Plasma Combustion Ignition System. IEEE Transactions on Plasma Science 2019;47(1):410–418. URL: https://ieeexplore.ieee.org/document/8579114/. doi:10.1109/TPS.2018.2882830.

[49] Scarcelli, R., Wallner, T., Som, S., Biswas, S., Ekoto, I., Breden, D., et al. Modeling non-equilibrium discharge and validating transient plasma characteristics at above-atmospheric pressure. Plasma Sources Science and Technology 2018;27(12):124006. URL: http://stacks.iop.org/0963-0252/27/i=12/a=124006?key=crossref.130175248ec9c49aa3fd6e65487b98b9. doi:10.1088/1361-6595/aaf539.

[50] Scarcelli, R., Zhang, A., Wallner, T., Breden, D., Karpatne, A., Raja, L., et al. Multi-dimensional Modeling of Non-equilibrium Plasma for Automotive Applications. In: SAE Technical Papers; vol. 2018-April. 2018, p. 1–10. URL: http://www.sae.org/content/2018-01-0198/. doi:10.4271/2018-01-0198.

[51] Ebert, U., Montijn, C., Briels, T.M.P., Hundsdorfer, W., Meulenbroek, B., Rocco, A., et al. The multiscale nature of streamers. Plasma Sources Science and Technology 2006;15(2):S118–S129. URL: http://stacks.iop.org/0963-0252/15/i=2/a=S14?key=crossref.7155d333648ba9011d162625b47fd9d4. doi:10.1088/0963-0252/15/2/S14.

[52] Qin, J., Pasko, V.P.. On the propagation of streamers in electrical discharges. Journal of Physics D: Applied Physics 2014;47(43):435202. URL: http://stacks.iop.org/0022-3727/47/i=43/a=435202?key=crossref.dc43c9a3618fa22ee7b7a05a6f339014. doi:10.1088/0022-3727/47/43/435202.

[53] Starikovskiy, A., Aleksandrov, N.. Plasma-assisted ignition and combustion. Progress in Energy and Combustion Science 2013;39(1):61–110. URL: http://dx.doi.org/10.1016/j.pecs.2012.05.003http://linkinghub.elsevier.com/retrieve/pii/S0360128512000354. doi:10.1016/j.pecs.2012.05.003.

[54] Burrows, J., Mixell, K.. Analytical and Experimental Optimization of the Advanced Corona Ignition System. In: Günther, M., Sens, M., editors. Ignition Systems for Gasoline Engines; vol. 2. Cham: Springer International Publishing. ISBN 978-3-319-45503-7; 2017, p. 267–292. URL: http://link.springer.com/10.1007/978-3-319-45504-4{_}19. doi:10.1007/978-3-319-45504-4_17.

[55] Cimarello, A., Grimaldi, C.N., Mariani, F., Battistoni, M., Dal Re, M.A.. Analysis of RF Corona Ignition in Lean Operating Conditions Using an Optical Access Engine. In: SAE Technical Paper. 2017, p. 1–22. URL: http://papers.sae.org/2017-01-0673/. doi:10.4271/2017-01-0673.

[56] Cimarello, A., Cruccolini, V., Discepoli, G., Battistoni, M., Mariani, F., Grimaldi, C.N., et al. Combustion Behavior of an RF Corona Ignition System with Different Control Strategies. In: SAE Technical Paper. 2018, p. 1–19. URL: http://www.sae.org/content/2018-01-1132/. doi:10.4271/2018-01-1132.

[57] Sevik, J., Wallner, T., Pamminger, M., Scarcelli, R., Singleton, D., Sanders, J.. Extending

Lean and Exhaust Gas Recirculation-Dilute Operating Limits of a Modern Gasoline Direct-Injection Engine Using a Low-Energy Transient Plasma Ignition System. Journal of Engineering for Gas Turbines and Power 2016;138(11):112807. URL: http://gasturbinespower.asmedigitalcollection.asme.org/article.aspx?doi=10.1115/1.4033470http://dx.doi.org/10.1115/1.4033470. doi:10.1115/1.4033470.

[58] Marko, F., König, G., Schöffler, T., Bohne, S., Dinkelacker, F.. Comparative Optical and Thermodynamic Investigations of High Frequency Corona- and Spark-Ignition on a CV Natural Gas Research Engine Operated with Charge Dilution by Exhaust Gas Recirculation. In: Ignition Systems for Gasoline Engines. Cham: Springer International Publishing. ISBN 978-3-319-45503-7; 2017, p. 293–314. URL: http://link.springer.com/10.1007/978-3-319-45504-4http://link.springer.com/10.1007/978-3-319-45504-4{_}18. doi:10.1007/978-3-319-45504-4_18.

[59] Padala, S., Nagaraja, S., Ikeda, Y., Le, M.K.. Extension of Dilution Limit in Propane-Air Mixtures Using Microwave Discharge Igniter. X; 2017,URL: http://papers.sae.org/2017-24-0148/https://www.sae.org/content/2017-24-0148/. doi:10.4271/2017-24-0148.

[60] Briggs, T., Alger, T., Mangold, B.. Advanced Ignition Systems Evaluations for High-Dilution SI Engines. SAE International Journal of Engines 2014;7(4):2014–01–2625. URL: http://papers.sae.org/2014-01-2625/. doi:10.4271/2014-01-2625.

[61] Ricci, F., Zembi, J., Battistoni, M., Grimaldi, C.N., Discepoli, G., Petrucci, L.. Experimental and Numerical Investigations of the Early Flame Development Produced by a Corona Igniter. In: SAE Technical Paper Series; vol. 1. 2019,URL: https://www.sae.org/content/2019-24-0231/. doi:10.4271/2019-24-0231.

[62] Pineda, D.I., Wolk, B.M., Chen, J.Y., Dibble, R.W.. Application of Corona Discharge Ignition in a Boosted Direct-Injection Single Cylinder Gasoline Engine: Effects on Combustion Phasing, Fuel Consumption, and Emissions. SAE International Journal of Engines 2016;9(3):2016–01–9045. URL: http://papers.sae.org/2016-01-9045/. doi:10.4271/2016-01-9045.

[63] Schenk, M., Schauer, F.X., Sauer, C., Weber, G., Hahn, J., Schwarz, C.. Challenges to the Ignition System of Future Gasoline Engines – An Application Oriented Systems Comparison. In: Ignition Systems for Gasoline Engines. Cham: Springer International Publishing; 2017, p. 3–25. URL: http://link.springer.com/10.1007/978-3-319-45504-4{_}1. doi:10.1007/978-3-319-45504-4_1.

[64] Salvi, B., Subramanian, K.. Experimental investigation and phenomenological model development of flame kernel growth rate in a gasoline fuelled spark ignition engine. Applied Energy 2015;139:93–103. URL: http://dx.doi.org/10.1016/j.apenergy.2014.11.012https://linkinghub.elsevier.com/retrieve/pii/S0306261914011611. doi:10.1016/j.apenergy.2014.11.012.

[65] Discepoli, G., Cruccolini, V., Dal Re, M.A., Zembi, J., Battistoni, M., Mariani, F., et al. Experimental assessment of spark and corona igniters energy release. Energy Procedia 2018;148(Ati):1262–1269. URL: https://doi.org/10.1016/j.egypro.2018.08.001https://linkinghub.elsevier.com/retrieve/pii/S1876610218302807. doi:10.1016/j.egypro.2018.08.001.

[66] Loeb, L.B., Brown, S.C.. Electrical Coronas: Their Basic Physical Mechanisms. Physics Today 1966;19(1):109–111. URL: http://physicstoday.scitation.org/doi/10.1063/1.3047912. doi:10.1063/1.3047912.

[67] Chang, J.S., Lawless, P., Yamamoto, T.. Corona discharge processes. IEEE Transactions on Plasma Science 1991;19(6):1152–1166. URL: http://ieeexplore.ieee.org/document/125038/. doi:10.1109/27.125038.

[68] Heywood, J.B.. Internal Combustion Engine Fundamentals. Automotive technology series; McGraw-Hill; 1988. ISBN 9780071004992. URL: https://books.google.it/books?id=O69nQgAACAAJ.

[69] Cruccolini, V., Discepoli, G., Cimarello, A., Battistoni, M., Mariani, F., Grimaldi, C.N., et al. Lean combustion analysis using a corona discharge igniter in an optical engine fueled with methane and a hydrogen-methane blend. Fuel 2020;259(xxxx):116290. URL: https://doi.org/10.1016/j.fuel.2019.116290https://linkinghub.elsevier.com/retrieve/pii/S0016236119316448. doi:10.1016/j.fuel.2019.116290.

[70] Leonov, S., Opaits, D., Miles, R., Soloviev, V.. Time-resolved measurements of plasma-induced momentum in air and nitrogen under dielectric barrier discharge actuation. Physics of Plasmas 2010;17(11):113505. URL: http://aip.scitation.org/doi/10.1063/1.3494279. doi:10.1063/1.3494279.

[71] Enloe, C.L., Mangina, R.S., Font, G.I.. Normalized Electronegative Species Effects in the Dielectric-Barrier-Discharge Plasma Actuator. AIAA Journal 2016;54(7):2061–2068. URL: http://arc.aiaa.org/doi/10.2514/1.J054551. doi:10.2514/1.J054551.

[72] Toyota, H., Zama, S., Akamine, Y., Matsuoka, S., Hidaka, K.. Gaseous electrical discharge characteristics in air and nitrogen at cryogenic temperature. IEEE Transactions on Dielectrics and Electrical Insulation 2002;9(6):891–898. URL: http://ieeexplore.ieee.org/document/1115482/. doi:10.1109/TDEI.2002.1115482.

[73] Paschen, F.. Ueber die zum Funkenübergang in Luft, Wasserstoff und Kohlensäure bei verschiedenen Drucken erforderliche Potentialdifferenz. Annalen der Physik 1889;273(5):69–96. URL: http://doi.wiley.com/10.1002/andp.18892730505. doi:10.1002/andp.18892730505.

[74] Wolk, B.M., DeFilippo, A., Chen, J.Y., Dibble, R.W., Nishiyama, A., Ikeda, Y.. Enhancement of flame development by microwave-assisted spark ignition in constant volume combustion chamber. Combustion and Flame 2013;160(7):1225–1234. URL: http://dx.doi.org/10.1016/j.combustflame.2013.02.004https://linkinghub.elsevier.com/retrieve/pii/S0010218013000461. doi:10.1016/j.combustflame.2013.02.004.

[75] Aleksandrov, N.L., Bazelyan, E.M., Novitskii, G.A.. The effect of small O 2 addition on the properties of a long positive streamer in Ar. Journal of Physics D: Applied Physics 2001;34(9):1374–1378. URL: http://stacks.iop.org/0022-3727/34/i=9/a=314?key=crossref.28407993ac282f7aeb02ed120863015b. doi:10.1088/0022-3727/34/9/314.

[76] Uddi, M., Jiang, N., Mintusov, E., Adamovich, I.V., Lempert, W.R.. Atomic oxygen measurements in air and air/fuel nanosecond pulse discharges by two photon laser induced fluorescence. Proceedings of the Combustion Insti-

tute 2009;32(1):929–936. URL: `http://dx.doi.org/10.1016/j.proci.2008.06.049https://linkinghub.elsevier.com/retrieve/pii/S1540748908000734`. doi:10.1016/j.proci.2008.06.049.

[77] Babaeva, N., Naidis, G.. On streamer dynamics in dense media. Journal of Electrostatics 2001;53(2):123–133. URL: `https://linkinghub.elsevier.com/retrieve/pii/S0304388601001358`. doi:10.1016/S0304-3886(01)00135-8.

[78] Liu, N., Pasko, V.P.. Effects of photoionization on similarity properties of streamers at various pressures in air. Journal of Physics D: Applied Physics 2006;39(2):327–334. URL: `http://stacks.iop.org/0022-3727/39/i=2/a=013?key=crossref.aa346860991616ccf0dff1ac46248187`. doi:10.1088/0022-3727/39/2/013.

Appendix

From the proposed lumped-parameter model (fig. 3) the correlation between the supplied voltage V_s and the electrode voltage V_e determines the eq. 8 and eq. 9.

Let now

$$\begin{aligned} A &= R_1 + R_L - \omega^2 R_L L_1 \left(C_L + C_1\right) \\ B &= \omega \left(L_1 + R_1 R_L \left(C_L + C_1\right)\right) \\ C &= 1 - \omega^2 C_1 \left(R_1 R_L C_L + L_1\right) \\ D &= \omega \left(R_L C_L + R_1 C_1 - \omega^2 C_1 L_1 R_L C_L\right) \end{aligned} \tag{16}$$

and

$$\begin{aligned} \overline{\alpha} &= A + jB = r_1 e^{j\Theta_1} \\ \overline{\beta} &= C + jD = r_2 e^{j\Theta_2} \end{aligned} \tag{17}$$

then

$$\overline{Z}_1 + \overline{Z}_2 = \frac{\overline{\alpha}}{\overline{\beta}} = \frac{r_1}{r_2} e^{j(\Theta_1 - \Theta_2)} = \frac{r_1}{r_2} \cos\left(\Theta_1 - \Theta_2\right) + j\frac{r_1}{r_2} \sin\left(\Theta_1 - \Theta_2\right) \tag{18}$$

where

$$\begin{aligned} &\begin{cases} r_1 = \sqrt{A^2 + B^2} \\ \Theta_1 = 2\arctan\left(\dfrac{B}{\sqrt{A^2 + B^2} + A}\right) \end{cases} \\ &\begin{cases} r_2 = \sqrt{C^2 + D^2} \\ \Theta_2 = 2\arctan\left(\dfrac{D}{\sqrt{C^2 + D^2} + C}\right) \end{cases} \end{aligned} \tag{19}$$

The resonance condition for this system is:

$$\frac{r_1}{r_2} \sin\left(\Theta_1 - \Theta_2\right) = 0 \tag{20}$$

and this condition is respected if

$$\begin{cases} \Theta_1 - \Theta_2 = 0 & (case\ 1) \\ \Theta_1 - \Theta_2 = k \cdot \pi \quad , where\ k \in \mathbf{Z} & (case\ 2) \end{cases} \tag{21}$$

Case 1: $r_1 = \sqrt{A^2 + B^2} = 0 \Leftrightarrow A^2 + B^2 = 0$
Considering $A, B \in \mathbf{R}$, then

$$A^2 + B^2 = 0 \Leftrightarrow \begin{cases} A = 0 \\ B = 0 \end{cases} \tag{22}$$

$$\begin{cases} A = 0 & \Rightarrow \quad \omega_0 = \sqrt{\dfrac{R_1 + R_L}{R_L L_1 (C_L + C_1)}} > 0 \\ B = 0 & \Rightarrow \quad \omega_0 = 0 \end{cases} \tag{23}$$

Hence, the system the system has no solution for $r_1 = 0$.

Case 2a: $\Theta_1 - \Theta_2 = 0$, then

$$2\arctan\left(\frac{B}{\sqrt{A^2+B^2}+A}\right) = 2\arctan\left(\frac{D}{\sqrt{C^2+D^2}+C}\right) \tag{24}$$

therefore, the case *2a* resonance condition becomes

$$\frac{B\left(\sqrt{C^2+D^2}+C\right)}{D\left(\sqrt{A^2+B^2}+A\right)} = 1 \tag{25}$$

Case 2b: $\Theta_1 - \Theta_2 = k\pi$, where $k \in \mathbf{Z}$. Then,

$$2\arctan\left(\frac{B}{\sqrt{A^2+B^2}+A}\right) - 2\arctan\left(\frac{D}{\sqrt{C^2+D^2}+C}\right) = k\pi \tag{26}$$

$$\tan\left(2\arctan\left(\frac{B}{\sqrt{A^2+B^2}+A}\right) - 2\arctan\left(\frac{D}{\sqrt{C^2+D^2}+C}\right)\right) = \tan(k\pi) \tag{27}$$

Since $\tan(k\cdot\pi) = 0 \;\forall\; k \in \mathbf{Z}$, then

$$\begin{gathered} \tan\left(2\arctan\left(\frac{B}{\sqrt{A^2+B^2}+A}\right) - 2\arctan\left(\frac{D}{\sqrt{C^2+D^2}+C}\right)\right) = \\ \frac{\tan\left(2\arctan\left(\frac{B}{\sqrt{A^2+B^2}+A}\right)\right) - \tan\left(2\arctan\left(\frac{D}{\sqrt{C^2+D^2}+C}\right)\right)}{1+\tan\left(2\arctan\left(\frac{B}{\sqrt{A^2+B^2}+A}\right)\right) - \tan\left(2\arctan\left(\frac{D}{\sqrt{C^2+D^2}+C}\right)\right)} = 0 \end{gathered} \tag{28}$$

Therefore,

$$\tan\left(2\arctan\left(\frac{B}{\sqrt{A^2+B^2}+A}\right)\right) - \tan\left(2\arctan\left(\frac{D}{\sqrt{C^2+D^2}+C}\right)\right) = 0 \tag{29}$$

finally,

$$\frac{B\left(\sqrt{C^2+D^2}+C\right)}{D\left(\sqrt{A^2+B^2}+A\right)} = 1 \tag{30}$$

That is the same solution obtained for the case *2a* (eq. 25), therefore the solution is unique.